

# Supporting Information

## Atomic resolution differential-phase contrast STEM on ferroelectric materials: a mean-field approach

M. Campanini<sup>1\*</sup>, K. Eimre<sup>2</sup>, M. Bon<sup>1</sup>, C. A. Pignedoli<sup>2</sup>, M. D. Rossell<sup>1</sup>, R. Erni<sup>1</sup>

<sup>1</sup> Electron Microscopy Center, Swiss Federal Laboratories for Materials Science and Technology, Empa, Ueberlandstrasse 129, 8600 Dübendorf, Switzerland.

<sup>2</sup> nanotech@surfaces Laboratory, Swiss Federal Laboratories for Materials Science and Technology, Empa, Ueberlandstrasse 129, 8600 Dübendorf, Switzerland.

\*Corresponding author: marco.campanini@empa.ch

### S1. DFT Calculations

#### S1.1. Simulation Details

We optimized at a DFT level a 10 atoms  $R3c$   $\text{BiFeO}_3$  (BFO) cell, the minimum size allowing the simulation of a G-type antiferromagnetic ordering. [1] PAW pseudopotentials [2] described the core electrons, while a plane-wave basis set the valence. The exchange-correlation was approximated by the PBESol functional. [3] A Hubbard correction of 2 eV was applied to Fe atoms to catch the proper localization of the  $f$ -orbitals. [4] We set the energy cut-offs of 100 Ry (wave function) and 800 Ry (charge density) and a  $k$ -point grid of  $8 \times 8 \times 8$ , including the  $\Gamma$ -point.

We replicated the optimized  $R3c$  cell to generate the hexagonal supercell constituted by 60 atoms and represented in Fig. S1 (left), for which we run a DFT wavefunction optimization. We set the energy cut-offs of 150 Ry (wave function) and 3500 Ry (charge density) and a  $k$ -point grid of  $8 \times 5 \times 3$ , including the  $\Gamma$ -point. The high cutoff value was chosen to obtain a precise, high-density numerical grid for the calculated charge density.

All calculations were run using Quantum ESPRESSO (QE) code. [5,6]



**Figure S1** *Left*: the system simulated with QE code. Color code for the atom kind: Purple=Bi, Orange=Fe, Red=O. Arrows indicate the collinear spin configuration simulated. Rectangular Cell (Å):  $a=9.66$ ,  $b=5.58$ ,  $c=13.86$ . *Right*: 3D Electron Localization Function (ELF) from QE calculation. Isovalue=0.4. In green, the signal of the lone pair for the central Bi atom is highlighted. The system is oriented along the pseudo-cubic [001] zone axis (corresponding to the  $[4\ 2\ -1]$  of the  $R3c$  structure).

## S1.2. The Electronic Structure Description

The electron localization function (ELF) gives insight on the electron lone-pair present at the Bi sites, responsible for the non-centrosymmetric BFO structure and hence for its ferroelectricity. In agreement with previous studies, [7] this electronic feature of the system is properly described by the QE-calculation, although it is not visible in the charge density plot and the electrostatic potential (Fig. S1, right).

## S1.3. From Pseudopotential Calculations to All-Electron Electrostatic Potential

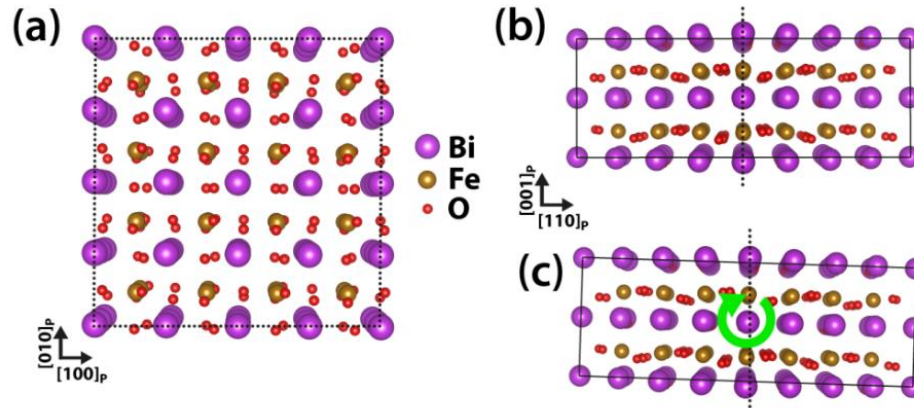
QE calculation gives rise to an electrostatic potential that does not properly describe the core-electrons, because of the use of pseudopotentials. In this work, a correct description of the core-region must be taken into account, because of its role in the scattering process. Starting from the valence charge density, QE can reconstruct the all-electron charge density, using information contained in the PAW pseudopotential (plot\_num=21 for pp.x input). We calculated this charge density on a real-space 200x360x500 grid. The core-electron charge density was not accurately represented due to the use of the finite grid. For this reason, we normalized it in the grid points around nuclei to obtain the correct integrated total charge. This was done by investigating the grid points corresponding to the position of the nuclei of the element, filtering out the anomalous values (differing more than 1 standard deviation) and setting the values to the mean. This procedure resulted in a total integrated charge off by only 0.3%, which we fixed by a global scaling.

In order to obtain the total electrostatic potential due to nuclei and the obtained electronic charge from QE, we employed the method of Ewald summation. [8] The potential due to nuclear charge was calculated in real space. The nuclear charge was represented by a Gaussian charge with  $\sigma=0.003$  a.u. which is compatible with the IAM potential cutoffs and produces an equivalent nuclear apex value for the final potential. The screening Gaussian charge used in Ewald was chosen according to the minimum image convention to have  $\sigma=1.0$  a.u. The potential due to the electronic charge (and the screening Gaussians) was calculated by numerically solving the Poisson equation via fast Fourier transforms. The final potential was shifted such that the lowest value in the unit cell was zero.

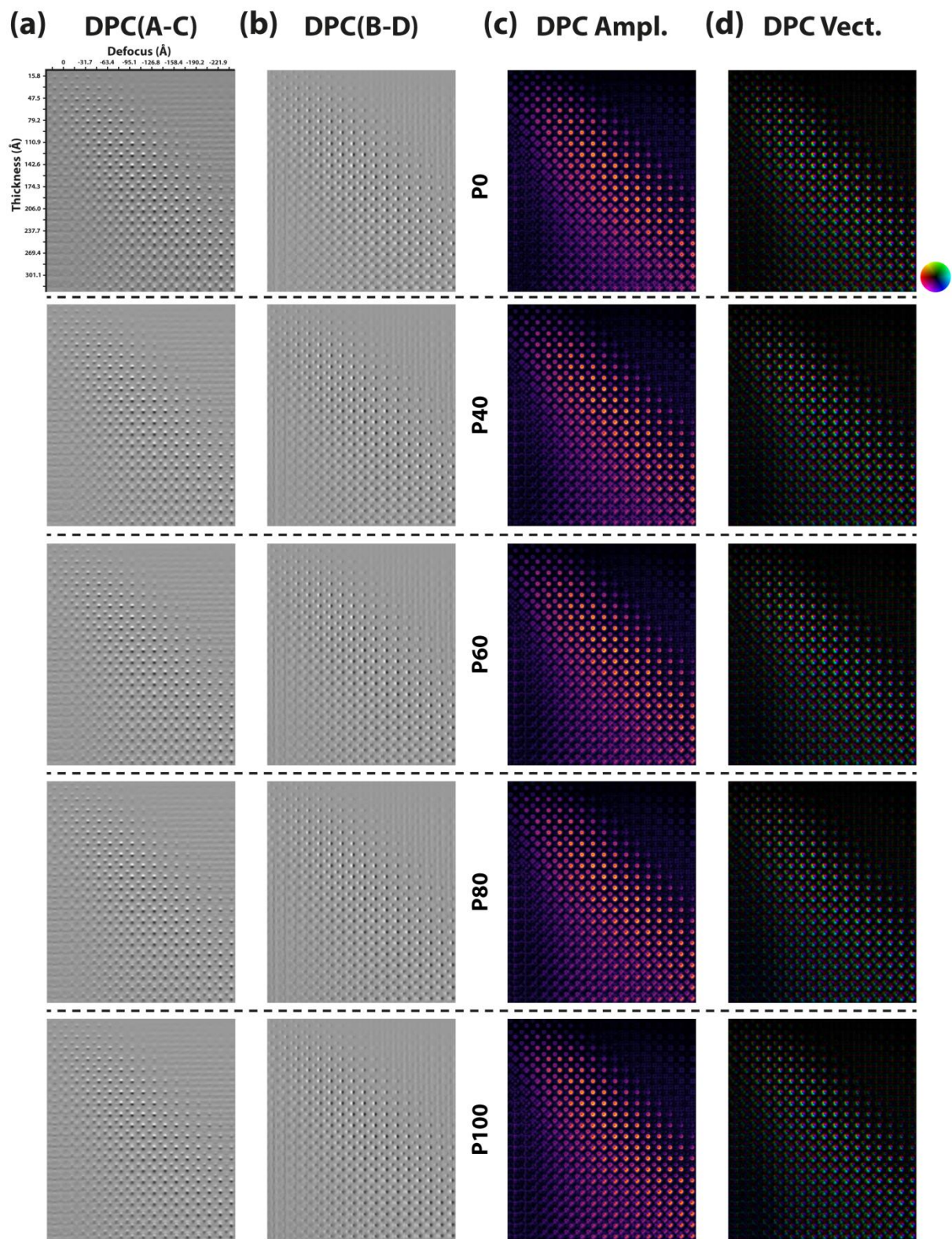
To obtain the projected potential, we first rotated the 3D total electrostatic potential to the correct orientation via trilinear interpolation. To reduce the inaccuracies caused by the finite real-space grid, we symmetrized the potential in a sphere of radius 0.20 Å around each nucleus and averaged this region for nuclei of the same kind (such that each nucleus of the same element has the same symmetric potential in a sphere of 0.20 Å). This happens so close to the nucleus that it does not affect the valence electrons or the region where the lone pair is located. Finally, the potential was projected on slices each containing one atomic layer.

The numerical tools to perform the potential calculation with Ewald and the rotation, symmetrization, and projection are included with the publication.

## S2. Specimen tilt in IAM multislice simulations

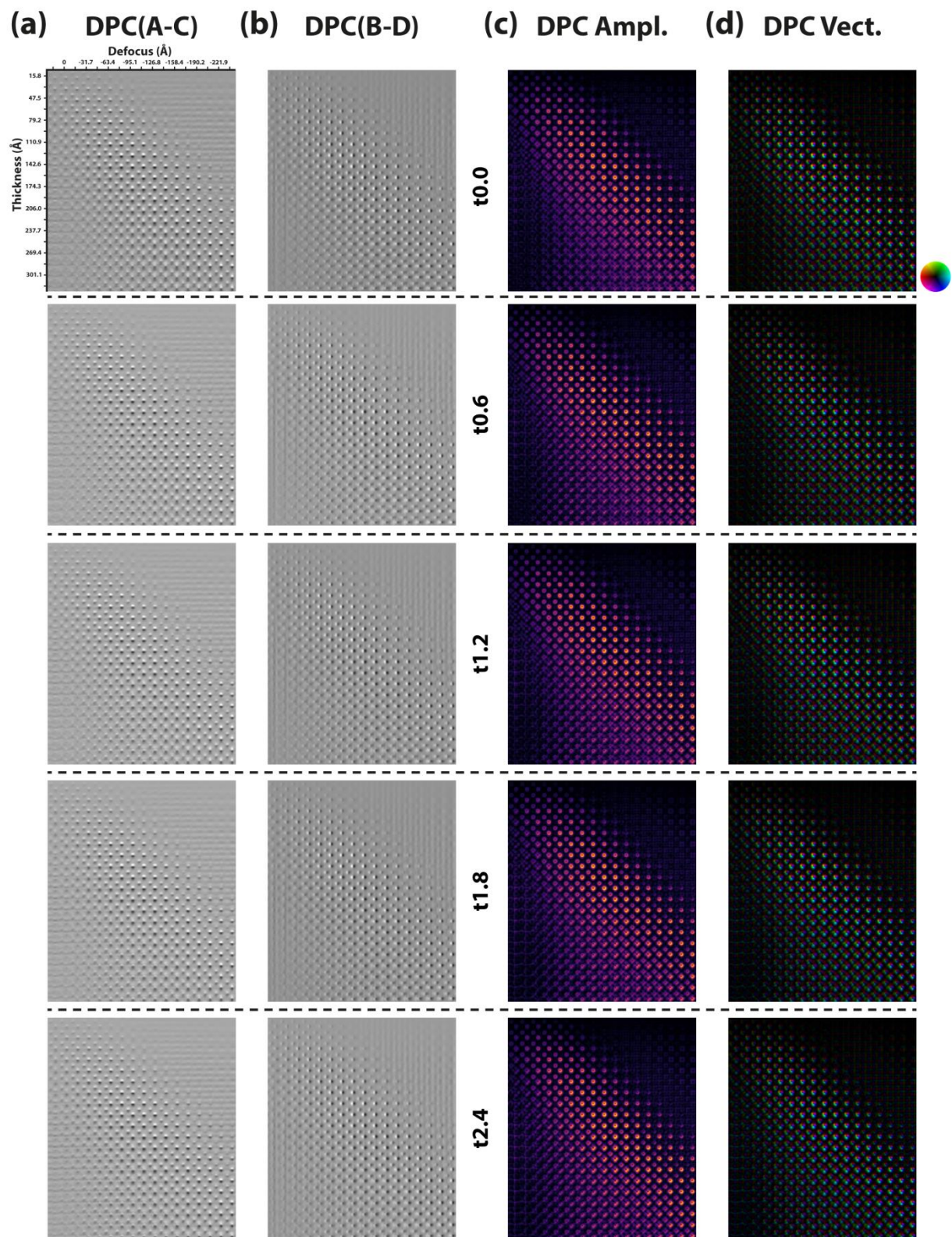


**Figure S2.** (a) BiFeO<sub>3</sub> crystal structure used for the generation of the projected potential in the IAM multislice simulations viewed along the  $[001]_p$  direction. (b,c) Crystal structure viewed along the  $[1-10]_p$  direction, before and after the application of a crystal rotation. The structure in (c) has been rotated by  $2^\circ$  to enhance the visibility of the tilted condition.



**Fig. S3.** The thickness and defocus series of DPC-STEM signals for different polarization values ( $P=0, 40, 60, 80, 100 \mu\text{C cm}^{-2}$ ). The thickness and defocus ranges are the same for each plot. (a), (b) Differential signals, (c) DPC amplitude, (d) vector plot. The HSV color wheel gives the direction and intensity of the electric field for the vector plot.





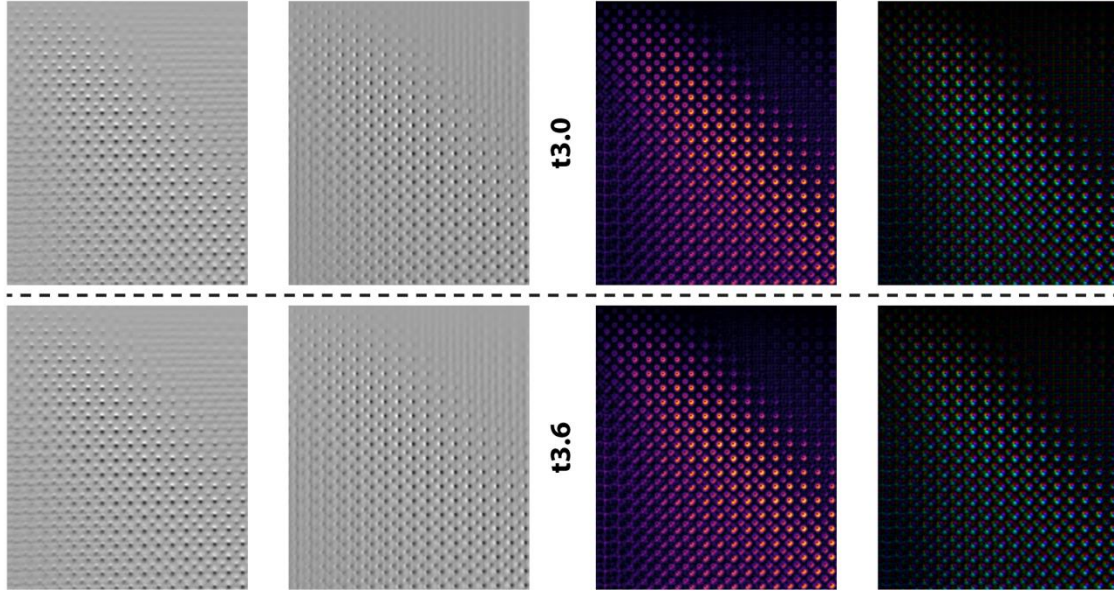


**Fig. S4.** The thickness and defocus series of DPC-STEM signals for different tilt angles ( $t = 0, 0.6, 1.2, 1.8, 2.4, 3.0, 3.6$  mrad). The thickness and defocus ranges are the same for each plot. (a), (b) Differential signals, (c) DPC amplitude, (d) vector plot. The HSV color wheel gives the direction and intensity of the electric field for the vector plot.

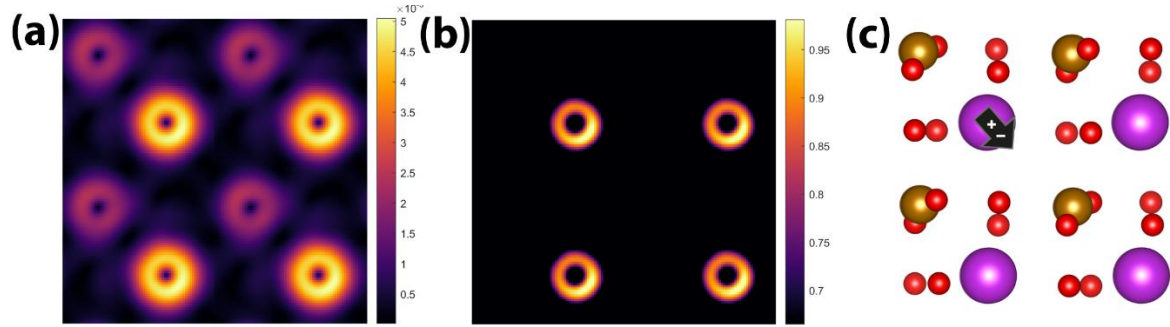


**Fig. S5.** (a) High-resolution DPC-STEM amplitude of  $\text{BiFeO}_3$  structure with thickness  $z = 20.54$  nm and defocus  $\Delta f = -174$  Å. In order to properly capture the fine details due to the microscopic dipole, the simulation was performed setting the real space resolution to  $0.06$  Å/pixel. (b) Equalized image showing the very small contribution of the unit cell dipole on the electric field of the Bi column. (c) Scheme of the  $\text{BiFeO}_3$  structure and sketch of the electric dipole. The plus and minus signs are plotted on the positions of the positive and negative center of charges, respectively.

## References

- [1] J. K. Shenton, D. R. Bowler, and W. L. Cheah, Effects of the Hubbard U on Density Functional-Based Predictions of BiFeO<sub>3</sub> properties *J. Phys. Condens. Matter* **29**, 445501 (2017).
- [2] P. E. Blöchl, Projector Augmented-Wave Method *Phys. Rev. B* **50**, 17953 (1994).
- [3] J. P. Perdew, A. Ruzsinszky, G. I. Csonka, O. A. Vydrov, G. E. Scuseria, L. A. Constantin, X. Zhou, and K. Burke, Restoring the Density-Gradient Expansion for Exchange in Solids and Surfaces *Phys. Rev. Lett.* **100**, 136406 (2008).
- [4] R. J. Zeches, M. D. Rossell, J. X. Zhang, A. J. Hatt, Q. He, C.-H. Yang, A. Kumar, C. H. Wang, A. Melville, C. Adamo, G. Sheng, Y.-H. Chu, J. F. Ihlefeld, R. Erni, C. Ederer, V. Gopalan, L. Q. Chen, D. G. Schlom, N. A. Spaldin, L. W. Martin, and R. Ramesh, A Strain-Driven Morphotropic Phase Boundary in BiFeO<sub>3</sub>. *Science* **326**, 977 (2009).
- [5] P. Giannozzi, S. Baroni, N. Bonini, M. Calandra, R. Car, C. Cavazzoni, D. Ceresoli, G. L. Chiarotti, M. Cococcioni, I. Dabo, A. Dal Corso, S. De Gironcoli, S. Fabris, G. Fratesi, R. Gebauer, U. Gerstmann, C. Gougoussis, A. Kokalj, M. Lazzeri, L. Martin-Samos, N. Marzari, F. Mauri, R. Mazzarello, S. Paolini, A. Pasquarello, L. Paulatto, C. Sbraccia, S. Scandolo, G. Sclauzero, A. P. Seitsonen, A. Smogunov, P. Umari, and R. M. Wentzcovitch, QUANTUM ESPRESSO: A Modular and Open-Source Software Project for Quantum Simulations of Materials *J. Phys. Condens. Matter* **21**, (2009).
- [6] P. Giannozzi, O. Andreussi, T. Brumme, O. Bunau, M. Buongiorno Nardelli, M. Calandra, R. Car, C. Cavazzoni, D. Ceresoli, M. Cococcioni, N. Colonna, I. Carnimeo, A. Dal Corso, S. De Gironcoli, P. Delugas, R. A. Distasio, A. Ferretti, A. Floris, G. Fratesi, G. Fugallo, R. Gebauer, U. Gerstmann, F. Giustino, T. Gorni, J. Jia, M. Kawamura, H. Y. Ko, A. Kokalj, E. Küçükbenli, M. Lazzeri, M. Marsili, N. Marzari, F. Mauri, N. L. Nguyen, H. V. Nguyen, A. Otero-De-La-Roza, L. Paulatto, S. Poncé, D. Rocca, R. Sabatini, B. Santra, M. Schlipf, A. P. Seitsonen, A. Smogunov, I. Timrov, T. Thonhauser, P. Umari, N. Vast, X. Wu, and S. Baroni, Advanced Capabilities for Materials Modelling with Quantum ESPRESSO *J. Phys. Condens. Matter* **29**, (2017).
- [7] P. Ravindran, R. Vidya, A. Kjekshus, H. Fjellvåg, and O. Eriksson, Theoretical Investigation of Magnetoelectric Behavior in BiFe O<sub>3</sub> *Phys. Rev. B - Condens. Matter Mater. Phys.* **74**, (2006).
- [8] D. Frenkel and B. Smit, Understanding Molecular Simulation (Computational Science Series, Vol 1).